Transactions on Electrical and Electronic Materials (2018) 19:417–422
https://doi.org/10.1007/s42341-018-0062-4

Online ISSN 2092-7592
Print ISSN 1229-7607

REGULAR PAPER

The Preparation of Fe_3O_4 Thin Film and Its Electrochemical Characterization for Li-Ion Battery

Mansoo Choi[1] · Sang-Hun Lee[2] · Yang-Il Jung[3] · Wang-Kyu Choi[1] · Jei-Kwon Moon[1] · Jihoon Choi[2] · Bum-Kyoung Seo[1] · Seon-Byeong Kim[1]

Received: 20 July 2018 / Revised: 20 August 2018 / Accepted: 5 September 2018 / Published online: 12 September 2018

Abstract
In this study, the Fe_3O_4 thin film was prepared as anode materials to simultaneously provide higher reversible Li^+ capacity compared to 2D materials with high cycle properties for lithium ion batteries. Nano-crystalline Fe_3O_4 thin film has been prepared by using an electron beam evaporation system followed by heat treatment. Electrochemical measurement showed that the as-fabricated Fe_3O_4 thin film showed the conventional charge–discharge voltage profiles of magnetite and good cycle performance. The initial reversible capacity of Fe_3O_4 thin film was maintained during the 100 cycles with no capacity fading in a potential range of 0.005–3.0 V (vs. Li^+/Li).

Keywords Ferrites · Oxide thin film · Electrochemical measurement · Energy storage

1 Introduction

Magnetite (Fe_3O_4) is a half-metallic metal oxide with the inverse spinel structure and space group *Fd3m* [1]. Recently, the iron-based materials can be used for their promising application to Li-ion batteries (LIBs) as anode materials owing to their low cost and low toxicity [2, 3]. Among these oxides, magnetite (Fe_3O_4) has been considered as anode materials for next LIBs because of its high capacity (928 mAh g^{-1}), natural abundance, and high electronic conductivity [4–6]. However, it can be possible that the poor rate capability and low cycle performance limit its further practical applications [6].

To date, many efforts have been reported to improve its drawbacks with increased durability, high cycle stability, and rate capability. For example, nano-sized Fe_3O_4-based electrode materials were prepared with various dimensions such as nanoparticles, nanosheets, and nanotubes [7–10]. It is noticed that 2D porous nanostructure is beneficial in order to achieve the high specific capacity and stable rate performance because of the large surface area for both electron and lithium ion transport [11]. The coating with conductive materials of oxide nanostructures is another method to improve the structural integrity and cycle performance. In the previous results, the carbon coating effectively buffer the strain caused by volume changes and prevent the aggregation during cycling [12]. For example, Zuo et al. [13] reported novel 2D carbon-encapsulated hollow Fe_3O_4 nanoparticles homogeneously anchored on graphene nanosheets as a high-rate LIBs anode material. In their architecture, the thin carbon shells can avoid the direct exposure of Fe_3O_4 nanoparticles to the electrolyte and preserve the structural and interfacial stabilization of Fe_3O_4 nanoparticles [13]. Even though a variety of good strategies for high electrochemical properties of Fe_3O_4 particles as anode material have been developed, the unique and novel material design for high cycling stability is still not satisfactory. So, new strategy or dimension architecture of electrode materials should be suggested to achieve the high performance of the Fe_3O_4.

Herein, we fabricated Fe_3O_4 thin film as anode materials to simultaneously provide a high discharge capacity with good cycle performance for LIBs. With the heat treatment, the Fe_3O_4 thin film deposited on stainless foil by using an

✉ Mansoo Choi
teracms@kaeri.re.kr

Seon-Byeong Kim
sbkim@kaeri.re.kr

[1] Decommissioning Technology Research Division, Korea Atomic Energy Research Institute, Daejeon 305-353, Korea

[2] Material Science and Engineering, Chungnam National University, Daejeon 34134, Korea

[3] LWR Fuel Technology Division, Korea Atomic Energy Research Institute, Daejeon 305-353, Korea

E-beam evaporator have been readily used as anode materials without further process, presenting improved performance compared to the conventional anodic Fe_3O_4 materials.

2 Experimental

The deposition of Fe_3O_4 thin film was prepared by following a published process [6]. Fe_3O_4 thin film deposited on stainless foil (SUS 304, thickness 25 μm) was prepared by using an electron beam evaporation system at room temperature. Fe_3O_4 pellet (purity 99.9%) was used as a target. The chamber was evacuated down to 2×10^{-6} Torr prior to deposition process. The deposition rate and thickness of Fe_3O_4 film were 2.6 Å s^{-1} and about 90 nm monitored by a thickness sensor during the evaporation process. The substrates were sputter-etched with Ar ions for 5 min prior to the deposition to remove any oxide layer on the surface. The Fe_3O_4 sample was sintered at 700 °C for 1 h in Ar atmosphere.

The morphology of the sample was investigated by a field emission scanning electron microscopy (S-4800, Hitachi) working at 30 kV and atomic force microscopy (Labram, Innova). The thin film X-ray diffraction (X-pert PRO MRD, Philips) pattern was conducted with Cu Kα radiation (λ = 1.5406 Å) operating at 40 kV and 30 mA between 10° and 90° at a scan rate of 0.01°, 2θ min^{-1}. Raman measurement (NTEGRA SPECTRA, NT-MDT) was conducted with a laser wavelength of 532 nm. The X-ray photoelectron spectroscopy (K-alpha, Thermo VG Scientific) analysis was performed and the binding energy was referenced to the C 1*s* peak from carbon at 284 eV.

The electrochemical performance of the Fe_3O_4 film was evaluated by 2032 coin cells assembled in a dry room. The Li metal was used as a counter and reference electrode. The 1.3 M $LiPF_6$ dissolved in ethylene carbonate (EC) and diethyl carbonate (DEC) (3:7 in volume) and polypropylene 2400 were also used as an electrolyte and separator, respectively. Galvanostatic charge–discharge was performed in a potential range of 0.005–3.0 V (vs. Li^+/Li) with an applied current density of 92.8 mA g^{-1}. The specific capacity of Fe_3O_4 electrode was based on the Fe_3O_4 electrode amount, which is calculated by Fe_3O_4 density (5 g cm^{-3}). The cyclic voltammetry (CV) was recorded at potential range of 0.005–3.0 V at a scan rate of 0.5 mV s^{-1}. All the electrochemical measurements were carried out at a room temperature.

3 Results and Discussion

The structure and phase purity of Fe_3O_4 thin film electrode sample are examined by X-ray diffraction (XRD). Figure 1 depicts the XRD patters of Fe_3O_4 powder and as-prepared

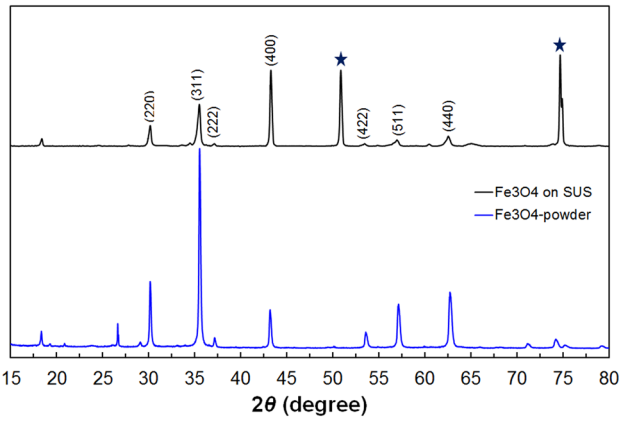

Fig. 1 XRD patterns of Fe_3O_4 powder and Fe_3O_4 thin film on SUS304 after heat treatment

Fe_3O_4 film. The main peaks (220, 311) of Fe_3O_4 film can be indexed on the basis of the cubic magnetite spinel phase (Fe_3O_4, *Fd3m* space group) [13]. The peak at 43.5° of Fe_3O_4 (400) overlapped (data not shown) with that of stainless steel. No additional impurity peak was observed, indicating the phase purity of Fe_3O_4 structure. The peaks denoted by star are related to the stainless steel.

The morphology and structure of Fe_3O_4 thin film was examined by field emission scanning electron microscopy (FE-SEM). Figure 2a, b show the morphologies of Fe_3O_4 film on the stainless foil. Before annealing sample (Fig. 2a), the surface of Fe_3O_4 film shows small grains and there is no other film phase after deposition. Also any peaks related to the Fe_3O_4 were not shown in XRD analysis. However, the strain of as deposited Fe_3O_4 thin film increased after annealing process. As shown in Fig. 2b, the Fe_3O_4 film showed different morphology. The small grains in the as-deposited increased in magnitude after annealing, suggesting that the film may be undergoing change of orientation [6]. Figure 2c shows the cross-section image of Fe_3O_4 thin film and the thickness of Fe_3O_4 film was about 90 nm (deposited on indium tin oxide glass). The atomic force microscopy (AFM) is also used to observe the surface roughness of Fe_3O_4 thin film. Figure 2d shows the thin-film phase image and height images of Fe_3O_4 surface after heating at 700 °C. The root-mean-squared roughness of Fe_3O_4 thin film (from 12 to 21 nm after heat treatment) was increased compared to as-deposited Fe_3O_4 thin-film in agreement with the SEM result.

The element distribution of each element in Fe_3O_4 film was observed energy dispersive X-ray spectroscopy (EDS) elemental mapping method. The EDS mapping images of iron and oxygen elements reveal that each element was uniformly dispersed (Fig. 3).

In order to evaluate the chemical state and composition of Fe_3O_4 film, Raman and XPS analysis were carried out (as illustrated in Fig. 4). As shown in Fig. 4a, Raman spectrum

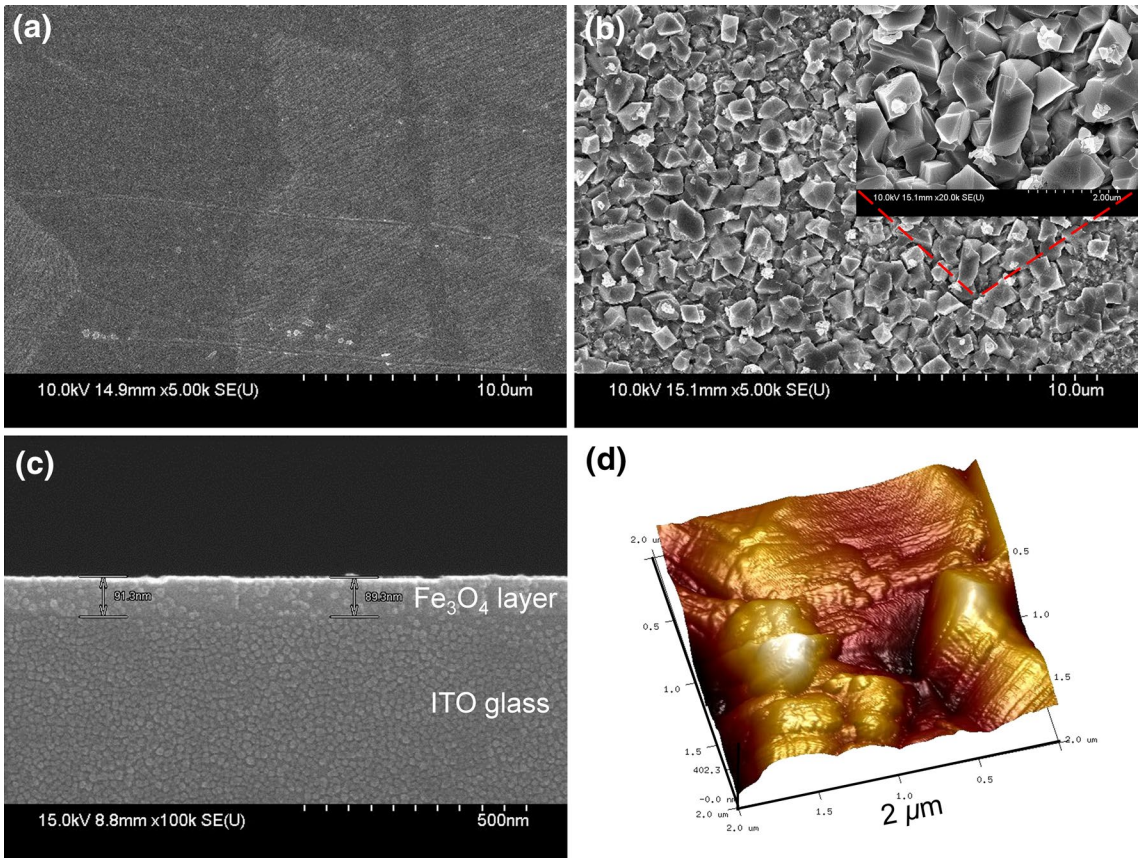

Fig. 2 SEM images of the Fe_3O_4 thin film; before (**a**) and after heat treatment (**b**), cross-sectional view of Fe_3O_4 thin film (**c**), AFM image of Fe_3O_4 thin film after heat treatment (**d**), respectively

of Fe_3O_4 film showed the characteristic peaks at 534 and 660 cm^{-1}, respectively, which is attributed to the T_{2g} and A_{1g} vibration mode of magnetite [14]. It is indicating that as-deposited thin film was composed of the Fe_3O_4 phase. Figure 4b shows the XPS spectra of Fe_3O_4 thin film. In the case of the iron, the Fe 2*p* peak is always split into two due to spin–orbit coupling [15]. No binding energy peak at 706. 6 eV, which is characteristic of metallic Fe $2p_{3/2}$ was observed [6]. Before the heat treatment of as-deposited Fe_3O_4 thin film, the additional satellite peak at ~719 eV could be observed. It could be attributed to the formation of a tiny amount of FeOOH confined on the top of the surface [15]. However, this peak was removed after heat treatment. The presence of Fe^{2+} and Fe^{3+} (1:1 ratio) reveals the equal presence of both satellites and thus an unresolved structure between the two spin–orbit components [16]. Therefore, the absence of resolved satellite peak is characteristic of the Fe_3O_4 layer [16].

The electrochemical performance of as-fabricated Fe_3O_4 thin was evaluated as anode materials by charge–discharge process with coin cell. Figure 5a depicts the first two CV profiles of Fe_3O_4 thin films in the potential range of 0.005–3 V at scan rate of 0.5 mV s^{-1}. Three redox peaks were observed during the oxidation and reduction reaction, suggesting the similar charge–discharge process according to the Fe_3O_4-based anodes [17–20]. The peak at 0.6 V is corresponded to the reduction of Fe^{3+} and Fe^{2+} to Fe^0 and the formation of amorphous Li_2O accompanied by irreversible side reaction related to the electrolyte decomposition [21, 22]. In Fig. 5a, the reduction peak intensity was decreased and shifted after the first cycle, indicating the occurrence of irreversible electrochemical reaction in the previous cycle [23]. However, the peak was observed at 1.78 V in the anodic sweep, corresponding to the oxidation of Fe^0 to Fe^{3+} with good reversibility of the electrochemical reaction [23–25]. Figure 5b shows the typical voltage profiles of Fe_3O_4 thin film at a constant current density of 92.8 mAh g^{-1} within a cut-off window of 0.005–3.0 V. The discharge voltage dropped from 1.5 to 0.8 V, which is ascribed to the oxidation of metallic Fe to Fe_3O_4. The distinct voltage plateau was observed at about 0.8 V during the discharge process, which is attributed to the transformations of Fe_3O_4 to a Li–Fe–O complex [17, 22]. The electrochemical reversible reaction with lithium can be summarized as;

$$Fe_3O_4 + 8e^- + 8Li^+ \Leftrightarrow 3Fe^0 + 4Li_2O$$

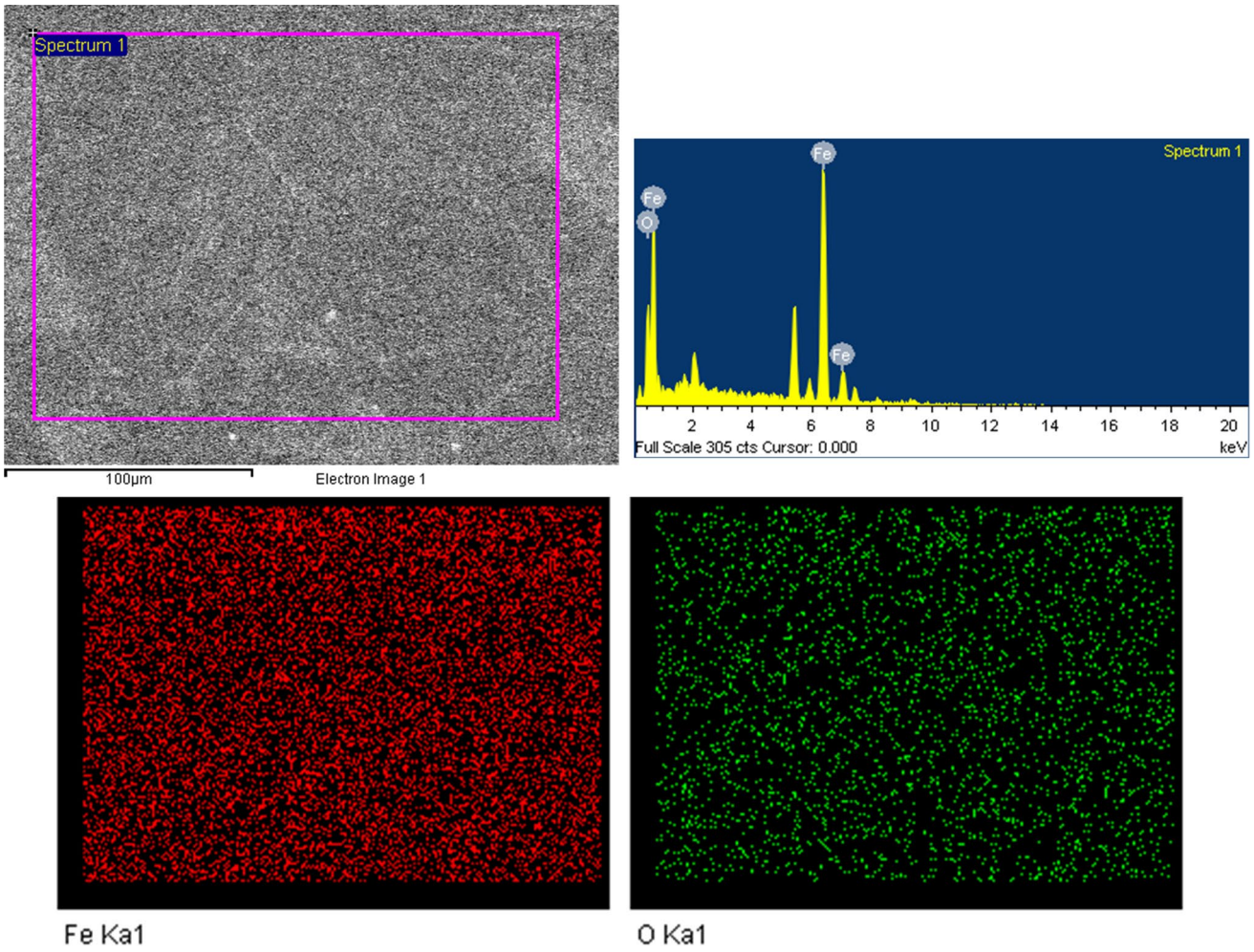

Fig. 3 Elemental analysis and EDS mapping image of Fe_3O_4 thin film

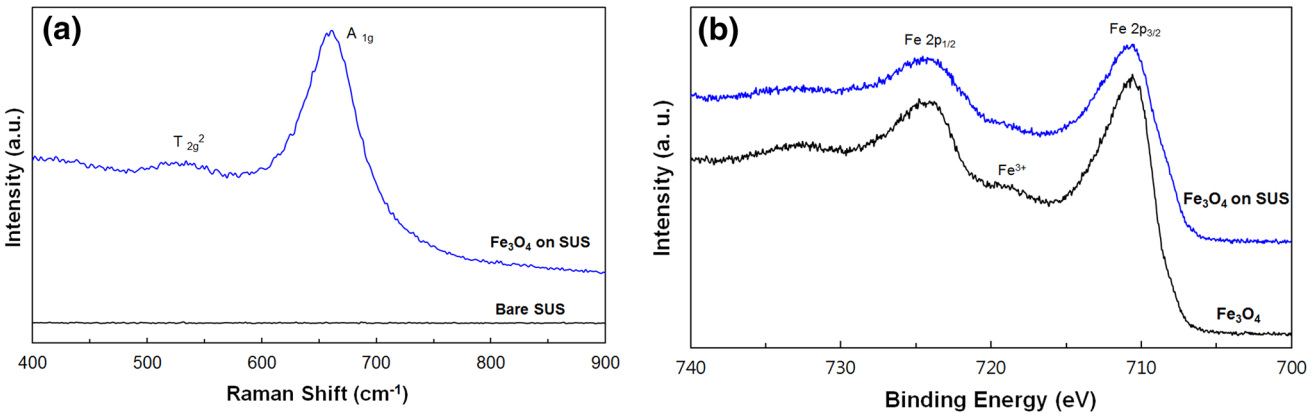

Fig. 4 **a** Raman spectra of Fe_3O_4 thin film after heat treatment and **b** XPS spectra of Fe_3O_4 thin film before and after heat treatment

The first discharge and charge capacity were found to be 1300 mAh g^{-1} and 900 mAh g^{-1}. The initial coulombic efficiency was about 70%, which is mainly caused by the solid-electrolyte interfacial layer (SEI layer), and initial irreversible formation of amorphous Li_2O caused by electrolyte decomposition [6]. Moreover, it is also the fact that large

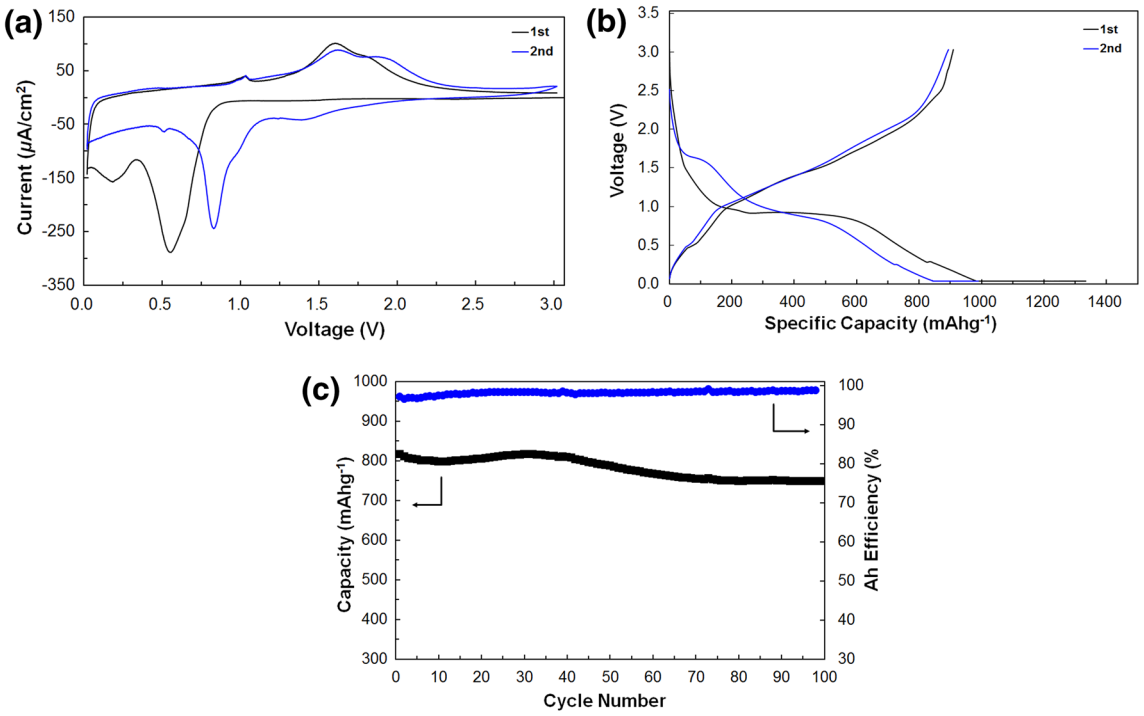

Fig. 5 Cyclic voltammetry curves (**a**), initial charge–discharge profiles (**b**), and cycling performance (**c**) of Fe_3O_4 thin film after heat treatment, respectively

capacity loss of Fe_3O_4 thin film in the first cycle is attributed to the conversion reaction of the nano-crystalline metal ferrite from M–O bond to Li_2O and the electrochemical driven formation of nanosized metallic grains [3]. In the second cycle, the columbic efficiency was improved to 93%.

The cycle performance of Fe_3O_4 thin film was further investigated for 100 cycles at a current density of 92.8 mA g^{-1}. Figure 5c depicted the cycling performance of Fe_3O_4 thin film with coulombic efficiency. Normally, the bare Fe_3O_4 materials showed the poor capacity retention. However, the capacity of Fe_3O_4 thin film was 748 mA g^{-1} after 100 cycles, which is 92% of the initial capacity (816 mA g^{-1}). Additionally, the coulombic efficiency of Fe_3O_4 thin film was over 98% for 100 cycles. The excellent cycling stability of electrode is ascribed to the sturdy construction of Fe_3O_4 thin film, which endures the volume expansion and aggregation of Fe_3O_4 during the charge–discharge [6].

The better electrochemical performance of Fe_3O_4 thin film electrode may be ascribed to that the Fe_3O_4 thin film has nano-crystalline structure and thinner thickness about 90 nm. It was reported that very thin film might allow that Li^+ ions could be diffused through the electrode more easily and enhanced the electronic conductivity from the substrate [26]. We thought that our fabricated Fe_3O_4 film was very thin and did not affect the resistance during charge–discharge process. In addition, the deposition of Fe_3O_4 thin film by e-beam evaporator followed by annealing process could fabricate more strong adhesive films onto the substrate than other deposition method [6].

4 Conclusion

Nano-crystalline Fe_3O_4 thin film has been prepared by using an electron beam evaporation system at room temperature. Electrochemical measurement showed that the as-fabricated Fe_3O_4 thin film showed the typical charge–discharge voltage profiles of magnetite and excellent cycling performance. The initial charge capacity of Fe_3O_4 thin film was 1300 mA g^{-1} at a current density of 92.8 mA g^{-1}, and remained about their capacity during 100 cycles (~92%). The better cycling stability is attributed to their structural stability. The nano-sized structure of thin film resulted in improved electrochemical performance and could be used as promising anode materials for Li-ion battery without any additives or other polymer binder.

Acknowledgements This work was supported by the Nuclear R&D Program (2017M2A8A5015144) funded by Ministry of Science and ICT.

References

1. Z. Zhang, S. Satpathy, Phys. Rev. B **44**, 13391 (1991)
2. J.-M. Tarascon, M. Armand, Nature **414**, 359 (2001)
3. Y.-N. NuLi, Q.-Z. Qin, J. Power Sources **142**, 292 (2005)
4. P.L. Tarascon, S. Mitra, P. Poizot, P. Simon, J.-M. Tarascon, Nat. Mater. **5**, 567 (2006)
5. H. Liu, G. Wang, J. Wang, D. Wexler, Electrochem. Commun. **10**, 1879 (2008)
6. M. Choi, S.-H. Lee, Y.-I. Jung, J.-J. Jung, J.-S. Park, W.-K. Choi, S.-Y. Park, H.-J. Won, J.-K. Moon, J. Choi, S.-B. Kim, J. Alloys Compd. **729**, 802 (2017)
7. L. Wang, L. Zhuo, C. Zhang, F. Zhao, Chem.-Eur. J. **20**, 4308 (2014)
8. H.G. Deng, S.L. Jin, L. Zhan, M.L. Jin, L.C. Ling, New Carbon Mater. **29**, 301 (2014)
9. Y.G. Zhu, J. Xie, G.S. Cao, T.J. Zhu, X.B. Zhao, RSC Adv. **3**, 6787 (2013)
10. K.Y. Xie, Z.G. Lu, H.T. Huang, W. Lu, Y.Q. Lai, J. Li, L.M. Zhou, Y.X. Liu, J. Mater. Chem. **22**, 5560 (2012)
11. D.Q. Liu, X. Wang, X.B. Wang, W. Tian, J.W. Liu, C.Y. Zhi, D.Y. He, Y. Bando, D. Golberg, J. Mater. Chem. A **1**, 1952 (2013)
12. K. Cheng, F. Yang, K. Ye, Y. Zhang, X. Jiang, J.L. Yin, G.L. Wang, D.X. Cao, J. Power Sources **258**, 260 (2014)
13. Y. Zuo, G. Wang, J. Peng, G. Li, Y. Ma, F. Yum, B. Dai, X. Guo, C.-P. Wong, J. Mater. Chem. A **4**, 2453 (2016)
14. O.N. Shebanova, P. Lazor, J. Solid State Chem. **174**, 424 (2003)
15. A. Grosvenor, B. Kobe, N. McIntyre, Surf. Interface Anal. **36**, 1637 (2004)
16. J.-B. Moussy, J. Phys. D Appl. Phys. **46**, 143001 (2013)
17. B. Lim, J. Jin, J. Yoo, S.Y. Han, K. Kim, S. Kang, N. Park, S.M. Lee, H.J. Kim, S.U. Son, Chem. Commun. **50**, 7723 (2014)
18. A.P. Hu, X.H. Chen, Q.L. Tang, B. Zeng, Ceram. Int. **40**, 14713 (2014)
19. C.X. Wang, G.J. Shao, Z.P. Ma, S. Liu, W. Song, J.J. Song, Electrochim. Acta **130**, 679 (2014)
20. Y.P. Gan, H.Q. Gu, H. Xiao, Y. Xia, X.Y. Tao, H. Huang, J. Du, L.S. Xu, W.K. Zhang, New J. Chem. **38**, 2428 (2014)
21. M. Latorre-Sanchez, A. Primo, H. Garcia, J. Mater. Chem. **22**, 31373 (2012)
22. Q. Zhou, Z.B. Zhao, Z.Y. Wang, Y.F. Dong, X.Z. Wang, Y. Gogotsi, J.S. Qiu, Nanoscale **6**, 2286 (2014)
23. M.M. Liu, J. Sun, J. Mater. Chem. A **2**, 12068 (2014)
24. S.M. Abbas, S. Ali, N.A. Niaz, N. Ali, R. Ahmed, N. Ahmad, J. Alloys Compd. **611**, 260 (2014)
25. H.B. Geng, Q. Zhou, J.W. Zheng, H.W. Gu, RSC Adv. **4**, 6430 (2014)
26. S.-W. Song, K.A. Striebel, R.P. Reade, G.A. Roberts, E.J. Carins, J. Electrochem. Soc. **150**, A121 (2003)